

Integer defects, flow localization, and bistability on curved active surfaces

Rushikesh Shinde¹, Raphaël Voituriez^{2,3}, Andrew Callan-Jones^{1,*}

¹ *Université Paris Cité and CNRS, Laboratoire Matière et Systèmes Complexes, F-75013 Paris, France*

² *Sorbonne Université and CNRS, Laboratoire Jean Perrin, F-75005 Paris, France and*

³ *Sorbonne Université and CNRS, Laboratoire de Physique Théorique de la Matière Condensée, F-75005 Paris, France**

(Dated: June 18, 2024)

Biological surfaces, such as developing epithelial tissues, exhibit in-plane polar or nematic order and can be strongly curved. Recently, integer (+1) topological defects have been identified as morphogenetic hotspots in living systems. Yet, while +1 defects in active matter on flat surfaces are well-understood, the general principles governing curved active defects remain unknown. Here, we study the dynamics of integer defects in an extensile or contractile polar fluid on two types of morphogenetically-relevant substrates : (1) a cylinder terminated by a spherical cap, and (2) a bump on an otherwise flat surface. Because the Frank elastic energy on a curved surface generically induces a coupling to *deviatoric* curvature, \mathcal{D} (difference between squared principal curvatures), a +1 defect is induced on both surface types. We find that \mathcal{D} leads to surprising effects including localization of orientation gradients and active flows, and particularly for contractility, to hysteresis and bistability between quiescent and flowing defect states.

Axi-symmetric (or very close to), active curved surfaces abound in living systems: the actin-myosin cortex underlying the cell membrane [1, 2], and multi-cellular, epithelial structures such as tissue invaginations within the embryo and developing secretory glands are a few examples [3]. Orientational order, either polar or nematic, and active behavior is also found at the sub-cellular and tissue scales, and topological defects occur and have biological relevance [4–7].

For example, integer defects have been identified as morphogenetic organizing centers [5, 8], and are associated with outgrowths such as tentacles and the head in *Hydra* [8, 9]. It has also been found *in vitro* that a +1 defect within a flat, confined cell or bacterial monolayer leads to out-of-plane dynamics [10–12]. These studies suggest a close connection between active +1 defects and non-flat geometries, yet little is known about the underlying physical principles [13, 14]. Given the deep connection between curvature and topological defects in equilibrium ordered surfaces [15, 16], it is reasonable to expect that the active case presents an even deeper field of study.

Integer defects on flat, two-dimensional active fluids are known to be susceptible to flow-order instability. *In vitro* experiments in which a +1 defect in a myoblast monolayer was imprinted by boundary conditions (BCs) within a circular region revealed transitions between non-flowing, aster and flowing spiral defects [10], confirming a theoretical prediction [17]. Spiral flows were found to be accompanied by mound formation. A simulation study has been carried out to model this type of behavior [14], but analytical approaches to shed light on the fundamental physics are so far lacking.

Coinciding with recent advances in imposing substrate curvature on cultured cell monolayers [18–20], a few studies have modeled how fixed, but tunable curvature im-

pacts spontaneous flows in active nematic surfaces [21–23]. This approach is amenable to in-depth analytical studies, yet to date how substrate geometry influences +1 defect dynamics has not been systematically investigated [23].

In this letter, we consider an achiral active polar fluid on two prototypical, biologically-motivated axi-symmetric surfaces [3]: (1) a cylinder terminated by a spherical cap, and (2) a bump on an otherwise flat surface. The nematic elastic energy on curved surfaces includes a coupling to *deviatoric* curvature, \mathcal{D} [24], defined here as the difference between squared azimuthal and meridional curvatures. In contrast to flat surfaces where BCs may impose a net +1 topological charge, here we find that on axi-symmetric surfaces \mathcal{D} can serve a similar function.

Our results can be summarized as follows. On a type (1) surface we find an aster defect is stable with respect to contractility and unstable to extensility, like on a flat surface [17], but unlike there the activity threshold is independent of system size and the resulting spiral-like order and flows are localized to regions of small \mathcal{D} . On a type (2) surface, because of the region where $\mathcal{D} < 0$ (referred to here as the skirt), an aster is unstable at zero activity towards a spiral state and active flows are threshold-less, occurring for all non vanishing activity. While extensility leads to spatially extended flows, contractility localizes flows, and if high enough extinguishes them and restores the aster. Surprisingly, with increasing curvature of the skirt, the spiral-to-aster transition shifts from continuous to discontinuous and contractility-driven localised flows exhibit hysteresis.

We expect general biological relevance of this study. On epithelial bud and tubular structures closed at one end, cells or actomyosin fibers are found to be aligned or tilted either axially [25–28] or ortho-axially [29]. Such alignment necessarily encloses a +1 topological charge, making the physics predicted here available to these structures.

* andrew.callan-jones@u-paris.fr

Model: We consider an active polar fluid layer on a rigid, curved, axi-symmetric surface parametrized by the coordinates s^i , with $s^1 = s$ the meridional arc length coordinate $s^2 = \theta$ the azimuthal angle, as shown in Fig. 1. The local order is described by a tangent vector \mathbf{p} of unit length, and written as

$$\mathbf{p} = \sin \psi \hat{\mathbf{e}}_s + \cos \psi \hat{\mathbf{e}}_\theta. \quad (1)$$

Here, the unit tangent vectors $\hat{\mathbf{e}}_s$ and $\hat{\mathbf{e}}_\theta$ define the local orthonormal basis and $\psi(s, t)$ is the angle that \mathbf{p} makes with $\hat{\mathbf{e}}_\theta$; see Fig. 1 and SM, Sec. 1. Our goal here is to derive an equation for the dynamics of ψ arising from elastic and active, as well as other out-of-equilibrium terms. To do so, we first outline the geometry of the problem.

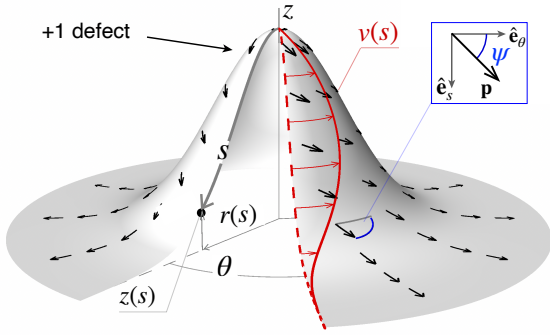


FIG. 1. **Illustration of a +1 defect in an active polar fluid on a surface of revolution.** The surface is defined by the coordinates $r(s)$ and $z(s)$. The polar field, is indicated by black arrows. Orthonormal flows $v(s)$ are represented by the red arrows and the red envelope curve.

Next, elastic effects are derived from a generalization of the two-dimensional Frank nematic free energy to include curvature. For simplicity, we only keep terms that are up-down symmetric and achiral and include two terms: the first, with modulus K , couples to intrinsic (Gaussian) curvature and consists in replacing partial derivatives with covariant ones [30, 31]; the second, with modulus K_{ex} , couples to extrinsic curvature. Thus, the energy is given by

$$\begin{aligned} F &= \int \left(\frac{K}{2} \nabla_i p^j \nabla^i p_j + \frac{K_{\text{ex}}}{2} p^j C_{ji} p_k C^{ki} \right) \sqrt{g} ds^1 ds^2 \\ &= \int \left(\frac{K}{2} \nabla_i p^j \nabla^i p_j + \frac{K_{\text{ex}}}{4} \mathcal{D} \cos(2\psi) \right) \sqrt{g} ds^1 ds^2. \end{aligned} \quad (2)$$

In the above, $\nabla_i p^j$ denotes the covariant derivative of the j component of \mathbf{p} with respect to the coordinate s^i , $i = 1, 2$; $g = \det(g_{ij})$ is the determinant of the metric tensor; and C_{ij} (C^{ij}) are the covariant (contravariant) components of the curvature tensor; see SI, Sec. 1 for details. We note that in the second line, dropping an

unimportant constant term, we have introduced the deviatoric curvature

$$\mathcal{D} = (C_\theta^\theta)^2 - (C_s^s)^2. \quad (3)$$

The extrinsic curvature term in Eq. 2, with two-fold symmetry about the normal, can be obtained from generic considerations of the bending energy of anisotropic membranes [24]. A related term with four-fold symmetry [32] has, for simplicity, been neglected [33]. We note that the two-fold term can also be obtained from a surface generalization of the Frank energy in the one constant approximation, which leads to $K_{\text{ex}} = K$ [34].

In the following we assume that $K_{\text{ex}} > 0$ [35]. It then follows that on a type (1) surface, where \mathcal{D} tends to a positive constant far from the apex, a +1 aster ($\psi = \pi/2$) is energetically favored. On a type (2) surface, the skirt region with $\mathcal{D} < 0$ energetically favors a +1 vortex ($\psi = 0$) defect. Thus, for an axi-symmetric (or very close to it) surface we expect a net +1 charge to be enclosed, whether the fluid is polar or nematic. Based on these considerations, we assume that $\psi = \psi(s)$, meaning that a +1 defect is found at the surface apex $s = 0$, and the problem is fully axi-symmetric.

Activity and other, passive out-of-equilibrium effects in the fluid are described here by a simple constitutive law for the in-plane non-equilibrium tension tensor [36]:

$$\mathbf{t} = \zeta \Delta \mu \mathbf{p} \otimes \mathbf{p} + 2\eta \mathbf{u} + \frac{\nu}{2} (\mathbf{h} \otimes \mathbf{p} + \mathbf{p} \otimes \mathbf{h}) + \frac{1}{2} (\mathbf{h} \otimes \mathbf{p} - \mathbf{p} \otimes \mathbf{h}), \quad (4)$$

where \otimes denotes the dyadic product. Note that this tensor is defined such that $\mathbf{t} \cdot \hat{\nu} dl$ is the internal force acting along a segment in the fluid of length dl and perpendicular to a unit tangent vector $\hat{\nu}$. In Eq. 4 $\zeta \Delta \mu$ is the coefficient of active tension, and positive in the contractile and negative in the extensile case; η is the in-plane shear viscosity and $\mathbf{u} = u^{ij} \mathbf{e}_i \otimes \mathbf{e}_j$, $u^{ij} = \frac{1}{2} (\nabla^i v^j + \nabla^j v^i)$ is the strain rate associated with the velocity field $\mathbf{v} = v^i \mathbf{e}_i$; ν is the flow-alignment parameter [37], and $\mathbf{h} = -\delta F / \delta \mathbf{p}$ is the molecular field; and the final term is the antisymmetric tension, as required by rotational invariance [36]. These equations are identical to those for a three-dimensional active polar gel [17, 38], with the difference that $\zeta \Delta \mu$ and η are surface quantities.

The mathematical formulation is completed by specifying the dynamics of \mathbf{p} ; for simplicity we only consider passive terms, and thus

$$\frac{D\mathbf{p}}{Dt} = \frac{\mathbf{h}}{\gamma} - \nu \mathbf{u} \cdot \mathbf{p}, \quad (5)$$

where $D\mathbf{p}/Dt = \partial \mathbf{p} / \partial t + \mathbf{v} \cdot \nabla \mathbf{p} - \boldsymbol{\omega} \times \mathbf{p}$ is the co-moving, co-rotational derivative of \mathbf{p} , and $\boldsymbol{\omega} = \frac{1}{2} \epsilon_{ij} \nabla^i v^j \mathbf{n}$ is the vorticity vector. Finally, γ is the rotational viscosity. We focus on the case where the fluid consists of rod-like particles; passive nematic arguments [39] suggest the alignment parameter $\nu < -1$, in agreement with measurements from different epithelial systems [40, 41]. This will be important in what follows.

We note that in Eq. 4 we have not included a pressure-like term, as we only require off-diagonal components of \mathbf{t} . A hypothesis on the compressibility of the layer is thus not required. Neglecting external forces tangent to the surface, such as friction or polar active self-propulsion [22], and admitting only the possibility of circumferential flows, $\mathbf{v} = v^\theta \mathbf{e}_\theta$, the axi-symmetry of the problem implies that the total torque along z acting on the sub-surface enclosed by a contour $r(s) = r$ is zero: $\dot{\mathbf{z}} \cdot \oint_r \mathbf{X} \times (\mathbf{t} \cdot \hat{\mathbf{e}}_s) dl = 0$. Here, we have neglected any contribution from a non-equilibrium moment tensor, and have noted that the above equality holds identically for the equilibrium tensions and moments because of rotational invariance about z [36]. We therefore find that the shear tension vanishes:

$$t^{s\theta} = 0. \quad (6)$$

This allows us to eliminate the strain rate $u^{s\theta}$ and therefore any explicit velocity dependence in Eq. 5. With some algebra, projecting Eq. 5 along $\mathbf{n} \times \mathbf{p}$ results in

$$\begin{aligned} \partial_t \psi = & \frac{1}{\tilde{\gamma}(\psi)} \left(K \nabla^2 \psi + \frac{1}{2} K_{\text{ex}} \mathcal{D} \sin(2\psi) \right) \\ & + \frac{\zeta \Delta \mu}{4\tilde{\eta}(\psi)} (1 + \nu \cos(2\psi)) \sin(2\psi), \end{aligned} \quad (7)$$

where $\tilde{\gamma}(\psi) > 0$ and $\tilde{\eta}(\psi) > 0$; see SM, Sec. 2 for details. Equation 7 is the dynamical equation for ψ we sought, and it has two key, curvature-dependent differences compared with its flat space analogue [17]: the Laplacian has been replaced with the Laplace-Beltrami operator, $\nabla^2 \psi \equiv \frac{1}{\sqrt{g}} \partial_j (\sqrt{g} g^{ij} \partial_i \psi)$, encoding intrinsic curvature; and the presence of the coupling to extrinsic curvature, here related to \mathcal{D} . These differences lead to surprising qualitative changes that we demonstrate below.

Linearized dynamics — localization by curvature: It will prove useful to have the linearized version of Eq. 7 about aster, $\psi = \pi/2 + \delta\psi$, and vortex, $\psi = \delta\psi$, defects. For small $\delta\psi$ we have

$$\frac{\partial \delta\psi}{\partial t} = \frac{K}{\gamma_\pm} \left(\nabla^2 \delta\psi \mp \frac{K_{\text{ex}}}{K} \mathcal{D} \delta\psi \right) + \frac{\zeta \Delta \mu (\nu \mp 1)}{2\eta} \delta\psi, \quad (8)$$

where $\gamma_\pm^{-1} \equiv \gamma^{-1} + (1 \mp \nu)^2 / 4\eta$, and the upper (lower) sign here and above is for an aster (vortex). We remark on the passing resemblance of this equation to the Schrödinger wave equation [42], with the extrinsic curvature term akin to an external potential. For constant \mathcal{D} , small deviations from aster order vary on a length scale

$$l^{-2} = \frac{\zeta \Delta \mu \gamma_+ (1 - \nu)}{2K\eta} + \frac{K_{\text{ext}}}{K} \mathcal{D}. \quad (9)$$

If l^{-2} is positive the above equation implies exponential decay of $\delta\psi$. In the linear regime flows induced by $\delta\psi$ will be seen to decay similarly.

Localized flows on a type (1) surface: The physics of an aster or vortex defect in a 2D, initially quiescent, active fluid of rod-shaped constituents confined to a disk of

diameter D can be summarized as follows [17]: a supercritical bifurcation occurs at a critical extensile activity $\zeta \Delta \mu_c \propto -D^{-2}$, beyond which the defect destabilizes towards a spiral state with active flows that span the disk. This picture is significantly changed when the substrate is curved.

We first consider the fluid to be bound to a spherocylinder of radius R , as illustrated in Fig. 2a. Far away from the cap and at a distance L along the cylinder the orientation is assumed fixed to be $\psi = \pi/2$ [43]. By symmetry the initial configuration is therefore aster-like. We look for the critical activity for an aster-to-spiral (A-S) transition. We show that above this value spiral order and the attendant flows are localized to the cap; a second transition occurs at higher extensile activity to the familiar bend-dominated distortion along the length of the cylinder (not shown; see Refs. [44, 45]). To find $\zeta \Delta \mu_c$, we consider the linearized equation, Eq. 8, with the upper signs. The deviatoric curvature is everywhere non-negative: on the hemispherical cap $\mathcal{D} = 0$ and on the cylindrical surface $\mathcal{D} = 1/R^2 = \text{const}$. It follows that the aster is linearly stable with respect to contractility, as on a flat surface [17] — using the quantum mechanical analogy, there are no “negative energy states”. Thus, aster instability only occurs for extensile activity, which is the case of interest for the rest of this section. A non-trivial stationary solution to Eq. 8 in analytical form can then be obtained:

$$\delta\psi = \begin{cases} P_n[\cos(s/R)], & 0 < s \leq R; \\ Ae^{-s/l_c} + Be^{s/l_c}, & R < s \leq L. \end{cases} \quad (10)$$

Here, A and B are unknown constants; P_n is the Legendre polynomial of order $n = (\sqrt{1 - 4\mathcal{Z}_c} - 1)/2$, $n \in \mathbb{R}$; and $\mathcal{Z}_c \equiv \zeta \Delta \mu_c (1 - \nu) \gamma_+ R^2 / 2\eta K = -n(n+1)$ is the dimensionless activity threshold. The length l_c , as defined in Eq. 9 and at threshold, is in the current geometry given by $l_c^{-2} = R^{-2} (\mathcal{Z}_c + K_{\text{ex}}/K)$. Applying the boundary condition $\delta\psi(s = L + \pi R/2) = 0$ and requiring continuity of $\delta\psi$ and $\partial_s \delta\psi$ at $s = \pi R/2$ allow determination of A , B , and \mathcal{Z}_c ; see Fig. 2b. For large L/l_c , $B \simeq 0$, and \mathcal{Z}_c is obtained by solving

$$(n+1)P_{n+1}(0) + \sqrt{K_{\text{ex}}/K - n(n+1)} P_n(0) = 0. \quad (11)$$

The first root, n_c , corresponding to the activity threshold, is less than 1, i.e., $\mathcal{Z}_c > -2$. For $K_{\text{ex}} = K$, $\mathcal{Z}_c \approx -0.53$; with increasing K_{ex}/K , $\mathcal{Z}_c \rightarrow -2$ (Fig. 2b). In this limit, the cylinder curvature completely screens $\delta\psi$, and spiral reordering is confined to the cap.

Above threshold the flow $v = \hat{\mathbf{e}}_\theta \cdot \mathbf{v}$ is non-zero and is obtained by integration of Eq. 6; see SM, Sec. 3. It vanishes at $s = 0$, is maximal along the hemispherical cap and decays exponentially along the cylinder with characteristic length, l ; see SM, Sec. 4. This exponential decay holds well-above threshold; see Fig. 2c. The steady state that results is akin to a bound state of a quantum particle with spatial extent l that depends on R but not on the system size L .

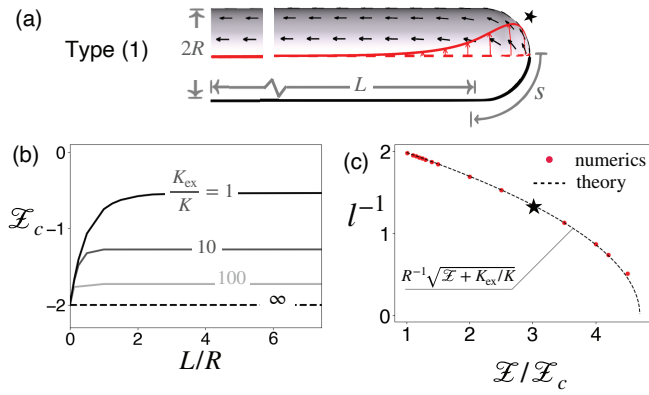


FIG. 2. **Spontaneous localized flow for extensile activity.** (a) Active polar fluid on a sphero-cylinder. Above $\zeta\Delta\mu_c$, $\delta\psi(s)$ and $v(s)$ are non-zero and decay exponentially. (b) Dimensionless activity threshold $\mathcal{Z}_c \equiv \zeta\Delta\mu_c(1-\nu)\gamma_+R^2/2\eta K$ versus L/R . (c) Decay length l^{-1} versus $\mathcal{Z} \equiv \zeta\Delta\mu(1-\nu)\gamma_+R^2/2\eta K$. Red points/Dashed line: numerical/analytical determination of l^{-1} . The numerical value is found from the slope of $\log v$ vs s (SI). The polarity and flow profiles in (a) were obtained for the value of \mathcal{Z} indicated by the star (*). Parameters : $\nu = -2, \gamma = \eta = 1, K_{\text{ext}}/K = 5, R = 1, L = 10$.

Localized flows on a type (2) surface: As a second illustration of the influence of extrinsic curvature on active +1 defects, we consider a hemispherical bump of radius R that is smoothly joined to a surrounding flat surface via a skirt (part of a torus) of major radius $R+\epsilon$ and minor radius ϵ ; see Fig. 3a. At any point on the skirt it can be readily shown that $\mathcal{D} \leq 0$. For simplicity, we assume that aster conditions, $\psi = \pi/2$, are imposed at the edge of the domain. This gives rise to frustrated order and bistability, which are new results in this work, though other choices of BCs can be studied [46]. Bistability is specific to frustration and would not occur for all choices. At zero activity, \mathcal{D} will drive the instability of an aster towards spiral-like order through a pitchfork bifurcation, if the skirt is sufficiently curved; see SM, Sec. 5. In the following, we assume that the zero activity state is spiral-like, with a non-vanishing gradient in ψ ; see Fig. 3b.

Turning on activity, the order profiles are altered: contractility tends to restore the aster state, and extensility expands the spiral state (Fig. 3b), consistent with their respective stabilizing and destabilizing effects on bend distortions [47]. Because of the director gradients in the passive state, the active flows are threshold-less [48], increase monotonically with extensility and non-monotonically with contractility, and vanishing at some value $\zeta\Delta\mu^*$, at which a spiral-to-aster (S-A) transition occurs (Figs. 3b, c). Furthermore, flows become more localized in the skirt with increasing contractility: away from the bump $v(s)$ decays exponentially with characteristic length given by Eq. 9 with $\mathcal{D} = 0$; see Figs. 3d and SM, Sec. 6. Overall, the possibility of contractility-generated active flows near integer defects, previously not found in flow-aligning ($\nu < -1$) active fluids on flat sur-

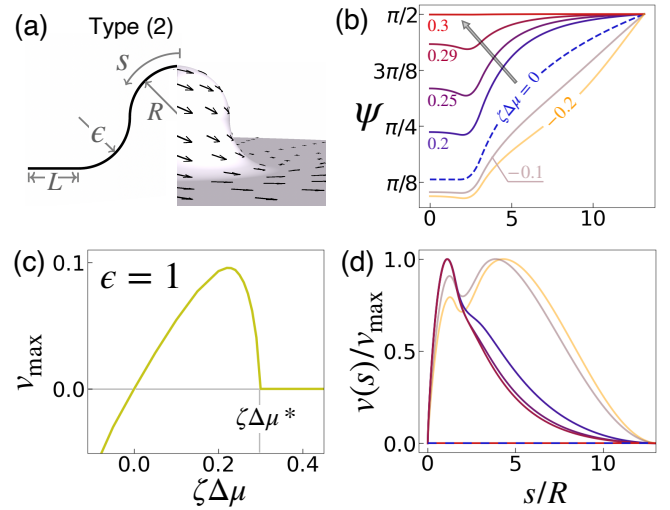


FIG. 3. **Spherical bump with low skirt curvature.** (a) Illustration of surface, with non-aster order in the zero activity state. (b) $\psi(s)$ profiles for different activity values. Contractility restores aster order, and the S-A transition is continuous. Extensility further destabilizes aster order. (c) The maximal value of $v(s)$ versus activity. It is defined as $v_{\text{max}} = \text{sgn}(\zeta\Delta\mu) \max[v(s)]$. Flows are threshold-less and smoothly vanish at a value $\zeta\Delta\mu^*$. (d) Contractile flows are localized whereas extensile flows span the system size. Parameters : $\nu = -2, \gamma = \eta = 1, K_{\text{ext}}/K = 1, R = \epsilon = 1, L = 10$.

faces [17], is due to the spiral order favored by $\mathcal{D} < 0$, and is traced back to the elastic energy dependence on extrinsic curvature.

First order transition at high $|\mathcal{D}|$: For greater inner curvature $1/\epsilon$ we were surprised to find that the S-A and A-S transitions become discontinuous. Starting in the spiral state — the yellow curve in Fig. 4, and referred to as S1—, with increasing contractility numerical integration of Eqs. 6 and 7 shows that the active flows first increase and then suddenly vanish at a value $\zeta\Delta\mu_1$ (Fig. 4a). For large $1/\epsilon$ the skirt favors vortex-like order, which is maintained on the bump (Fig. 4b). With increasing contractility, the angle ψ becomes close to $\pi/2$ everywhere on the flat part of the surface, and close to zero on the bump. This can be understood by noting from Eq. 8, that for $\nu < -1$, contractility stabilizes both aster *and* vortex order. At $\zeta\Delta\mu_1$ this geometry-induced frustration in the order is suddenly relieved, and the state S1 transitions to an aster. Hysteresis is also observed: as contractility is then decreased, the flows remain zero until a lower threshold $\zeta\Delta\mu_2$ at which aster order is continuously lost by a symmetry-breaking instability towards a different spiral state — referred to as S2—, and the order becoming vortex-like in the skirt (Fig. 4c). The final step is a snap-like transition of S2 to S1 at $\zeta\Delta\mu_3$ (Figs. 4a and c).

Our results for the bump surface are summarized in the phase diagram in Fig. 4d. The key feature is the tricritical point (T) that separates the regions where the A-S and S-A transitions are supercritical, from where they

are subcritical and bistability can occur. The bistable region, bounded by the curves I and III is further divided into subregions: between I and II the aster and S1 states coexist; and between II and III the two flowing states, S1 and S2, coexist. We note that our findings presented in Fig. 4d are not unique to our specific choice of bump surface in Fig. 3a. We found similar behavior, notably the presence of a tri-critical point in the phase behavior, in other surfaces of revolution, namely the revolved bump function and a bulb-tipped cylinder, which combines features of surfaces of types (1) and (2); see SM, Sec. 7. This suggests generic behavior shared by surfaces containing regions where $\mathcal{D} < 0$.

Discussion: We have studied +1 defects in active polar fluids on curved surfaces. We found that extrinsic curvature qualitatively changes the known physics of +1 active defects in flat 2D fluids: it provides spatial control of active flows and hysteresis between flowing and non-flowing states. Our work joins that of other recent studies on bistability in active nematics [21, 49].

We expect that the physics discovered here is biologically relevant. Rotational flow of cells in the bulb-shaped acinus of organoid-derived mammary epithelial tubes has

been observed, with an amplitude decaying with distance along the tube [28]. Our model might provide an explanation for this behavior.

Here, we have focused on active fluids that are polar by virtue of the assumption of an axi-symmetric, +1 defect imposed by substrate geometry. For simplicity we have not included terms in the equations of motion that break the $\mathbf{p} \rightarrow -\mathbf{p}$ symmetry. Furthermore, we have also not included substrate effects such as an active polar traction force [22], couplings that break up-down layer symmetry, and passive friction with the substrate [50]. Following other recent work [51], we have pursued a minimal model on a fixed surface to show how curvature augments the physics of active defects. Future work will more fully examine the parameter space that encompasses epithelial features not considered here.

Finally, we expect our work to be relevant to active nematics, as well. On axi-symmetric surfaces the curvature deviator \mathcal{D} , by favoring radial or circumferential alignment according to the Frank energy, Eq. 2, results in an enclosed +1 charge. It remains to be seen whether in such situations a single +1, two +1/2, or some other combinations of defects is selected.

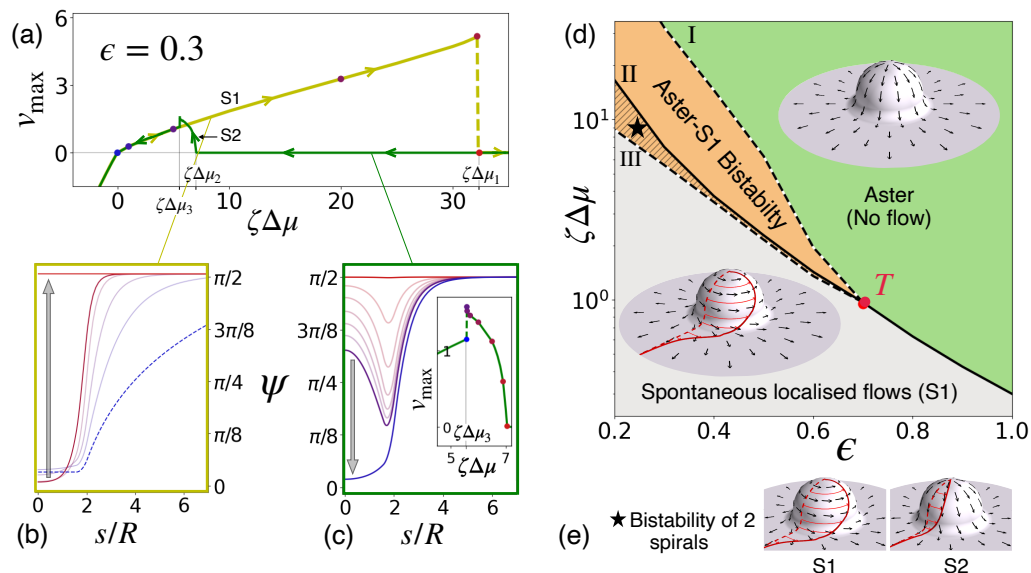


FIG. 4. **Spherical bump with high skirt curvature: bistability of spiral and aster states.** (a) The maximal value of $v(s)$ versus contractile activity. Hysteresis and discontinuous transitions are found numerically, and are shown here. (b) The $\psi(s)$ profiles, color-coded according to the points in (a), show a discontinuous S-A transition with increasing $\zeta\Delta\mu$. (c) The A-S is also discontinuous, but is preceded by a continuously deformed aster state prior to snapping. The corresponding values of v_{\max} along the the fin-shaped curve in (a) are given in the inset. (d) Phase diagram in the $\zeta\Delta\mu$ - ϵ plane. A tri-critical point (T) is shown, and for skirt radii less than ϵ_T the S-A and S-A transitions are first-order, indicating bistability of the spiral and aster. The dashed lines indicate discontinuous transitions, whereas the solid line continuous ones. (e) Close-up of polarity and flow profiles for S1 and S2 spiral states. Parameter values: $\nu = -2, \gamma = \eta = 1, K_{\text{ext}}/K = 1, R = 1, \epsilon = 0.3, L = 10$.

ACKNOWLEDGMENTS

RS acknowledges PhD funding from Ecole Doctorale Ile de France (EDPIF, contract number 1960999223S01).

RV is funded by ERC synergy grant SHAPINCELL-FATE. We also thank Jacques Prost for his careful reading and insightful comments on the manuscript.

- [1] G. Salbreux, G. Charras, and E. Paluch, *Trends in Cell Biology* **22**, 536 (2012).
- [2] M. Kelkar, P. Bohec, and G. Charras, *Curr Opin Cell Biol* **66**, 69 (2020).
- [3] D. J. Andrew and A. J. Ewald, *Dev Biol* **341**, 34 (2010).
- [4] A. Ardaševa and A. Doostmohammadi, *Nature Reviews Physics* **4**, 354 (2022).
- [5] L. Balasubramaniam, R.-M. Mège, and B. Ladoux, *Curr Opin Genet Dev* **73**, 101897 (2022).
- [6] M. J. Bowick, N. Fakhri, M. C. Marchetti, and S. Ramaswamy, *Phys. Rev. X* **12**, 010501 (2022).
- [7] S. Shankar, A. Souslov, M. J. Bowick, M. C. Marchetti, and V. Vitelli, *Nature Reviews Physics* **4**, 380 (2022).
- [8] Y. Maroudas-Sacks, L. Garion, L. Shani-Zerbib, A. Livshits, E. Braun, and K. Keren, *Nature Physics* **17**, 251 (2021).
- [9] Y. Ravichandran, M. Vogg, K. Kruse, D. J. Pearce, and A. Roux, *bioRxiv* (2024), 10.1101/2024.04.07.588499.
- [10] P. Guillamat, C. Blanch-Mercader, G. Pernollet, K. Kruse, and A. Roux, *Nat Mater* **21**, 588 (2022).
- [11] O. J. Meacock, A. Doostmohammadi, K. R. Foster, J. M. Yeomans, and W. M. Durham, *Nature Physics* **17**, 205 (2021).
- [12] M. Basaran, Y. I. Yaman, T. C. Yüce, R. Vetter, and A. Kocabas, *Elife* **11** (2022), 10.7554/eLife.72187.
- [13] L. Metselaar, J. M. Yeomans, and A. Doostmohammadi, *Phys Rev Lett* **123**, 208001 (2019).
- [14] L. A. Hoffmann, L. N. Carenza, J. Eckert, and L. Giomi, *Sci Adv* **8**, eabk2712 (2022).
- [15] M. J. Bowick and L. Giomi, *Advances in Physics* **58**, 449 (2009), <https://doi.org/10.1080/00018730903043166>.
- [16] A. M. Turner, V. Vitelli, and D. R. Nelson, *Rev. Mod. Phys.* **82**, 1301 (2010).
- [17] K. Kruse, J. F. Joanny, F. Jülicher, J. Prost, and K. Sekimoto, *Phys. Rev. Lett.* **92**, 078101 (2004).
- [18] S. J. P. Callens, R. J. C. Uyttendaele, L. E. Fratila-Apachitei, and A. A. Zadpoor, *Biomaterials* **232**, 119739 (2020).
- [19] B. Schamberger, R. Ziege, K. Anselme, M. Ben Amar, M. Bykowski, A. P. G. Castro, A. Cipitria, R. A. Coles, R. Dimova, M. Eder, S. Ehrig, L. M. Escudero, M. E. Evans, P. R. Fernandes, P. Fratzl, L. Geris, N. Gierlinger, E. Hannezo, A. Iglič, J. J. K. Kirkensgaard, P. Kollmannsberger, L. Kowalewska, N. A. Kurniawan, I. Pantoniou, L. Pieuchot, T. H. V. Pires, L. D. Renner, A. O. Sageman-Furnas, G. E. Schröder-Turk, A. Sengupta, V. R. Sharma, A. Tagua, C. Tomba, X. Trepast, S. L. Waters, E. F. Yeo, A. Roschger, C. M. Bidan, and J. W. C. Dunlop, *Adv Mater* **35**, e2206110 (2023).
- [20] M. Luciano, C. Tomba, A. Roux, and S. Gabriele, *Nature Reviews Physics* , 1 (2024).
- [21] S. Bell, S.-Z. Lin, J.-F. Rupprecht, and J. Prost, *Phys Rev Lett* **129**, 118001 (2022).
- [22] A. Glentis, C. Blanch-Mercader, L. Balasubramaniam, T. B. Saw, J. d’Alessandro, S. Janel, A. Douanier, B. Delaval, F. Lafont, C. T. Lim, D. Delacour, J. Prost, W. Xi, and B. Ladoux, *Sci Adv* **8**, eabn5406 (2022).
- [23] F. Vafa and L. Mahadevan, *Phys Rev Lett* **129**, 098102 (2022).
- [24] W. Helfrich and J. Prost, *Phys Rev A Gen Phys* **38**, 3065 (1988).
- [25] B. Venzac, R. Madoun, T. Benarab, S. Monnier, F. Cayrac, S. Myram, L. Leconte, F. Amblard, J.-L. Viovy, S. Descroix, and S. Coscoy, *Biomicrofluidics* **12**, 024114 (2018).
- [26] Y. E. Sanchez-Corrales, G. B. Blanchard, and K. Röper, *Elife* **7** (2018), 10.7554/eLife.35717.
- [27] C. Pérez-González, G. Ceada, F. Greco, M. Matejčić, M. Gómez-González, N. Castro, A. Menendez, S. Kale, D. Krndija, A. G. Clark, V. R. Gannavarapu, A. Álvarez-Varela, P. Roca-Cusachs, E. Batlle, D. M. Vignjevic, M. Arroyo, and X. Trepast, *Nature Cell Biology* **23**, 745 (2021).
- [28] P. A. Fernández, B. Buchmann, A. Goychuk, L. K. Engelbrecht, M. K. Raich, C. H. Scheel, E. Frey, and A. R. Bausch, *Nat Phys* **17**, 1130 (2021).
- [29] C. M. Karner, R. Chirumamilla, S. Aoki, P. Igarashi, J. B. Wallingford, and T. J. Carroll, *Nat Genet* **41**, 793 (2009).
- [30] Nelson, D.R. and Peliti, L., *J. Phys. France* **48**, 1085 (1987).
- [31] T.C. Lubensky and Jacques Prost, *J. Phys. II France* **2**, 371 (1992).
- [32] B. L. Mbangwa, G. M. Grason, and C. D. Santangelo, *Phys Rev Lett* **108**, 017801 (2012).
- [33] The four-fold symmetry term is proportional to $(C_\theta^\theta - C_s^s)^2 \sin(4\psi)$ [32]. On a spherocylinder it does not introduce any new physics as compared with the $\mathcal{D} > 0$ term in Eq. 2. On the hemispherical bump, it is also of no consequence, since it does not distinguish between vortex and aster order, and thus does not impact the discussion in Fig. 4.
- [34] G. Napoli and L. Vergori, *Phys. Rev. Lett.* **108**, 207803 (2012).
- [35] (), the choice $K_{\text{ex}} > 0$ is grounded in energetic arguments for constituents that are elongated along \mathbf{p} [24, 32, 52]. Activity could make this coefficient negative, as has been supposed in order to rationalize observation of circumferential polar alignment on a cylindrical fiber [22].
- [36] G. Salbreux, F. Jülicher, J. Prost, and A. Callan-Jones, *Phys. Rev. Res.* **4**, 033158 (2022).
- [37] P.-G. De Gennes and J. Prost, *The physics of liquid crystals*, 83 (Oxford university press, 1993).
- [38] F. Jülicher, S. W. Grill, and G. Salbreux, *Reports on Progress in Physics* **81**, 076601 (2018).
- [39] W. Helfrich, *The Journal of Chemical Physics* **50**, 100 (1969), <https://pubs.aip.org/aip/jcp/article-pdf/50/1/100/18859946/100.1-online.pdf>.
- [40] C. Blanch-Mercader, P. Guillamat, A. Roux, and K. Kruse, *Phys Rev Lett* **126**, 028101 (2021).
- [41] B. Aigouy, R. Farhadifar, D. B. Staple, A. Sagner, J.-C. Röper, F. Jülicher, and S. Eaton, *Cell* **142**, 773 (2010).
- [42] J. J. Sakurai and J. Napolitano, *Modern quantum mechanics* (Cambridge University Press, 2020).
- [43] We note that for $L \gg R$ free boundary conditions on ψ do not qualitatively change the results to follow.
- [44] G. Napoli and S. Turzi, *Phys. Rev. E* **101**, 022701 (2020).
- [45] S. C. Al-Izzi and R. G. Morris, *Journal of Fluid Mechanics* **957**, A4 (2023).
- [46] The case of $\psi = 0$ conditions does not lead to new physics as compared with Ref. [17]. If we impose free conditions, $\partial_s \psi = 0$, we find that bistability between spiral and vor-

tex states occurs over a range of contractilities, similar to that between spiral and aster states, when $\psi = \pi/2$ is fixed at the boundary. For simplicity we focus on these latter conditions.

- [47] S. Edwards and J. Yeomans, *Europhysics letters* **85**, 18008 (2009).
- [48] R. Green, J. Toner, and V. Vitelli, *Physical Review Fluids* **2**, 104201 (2017).
- [49] I. Lavi, R. Alert, J.-F. Joanny, and J. Casademunt, “Nonlinear spontaneous flow instability in active nematics,” (2024), arXiv:2403.16841 [cond-mat.soft].
- [50] (), friction, with coefficient ξ , combines with layer viscosity η to yield the length $l_\eta = \sqrt{\eta/\xi}$. For phenomena occurring on lengths less than l_η , friction can be ignored.
- [51] F. Vafa, D. R. Nelson, and A. Doostmohammadi, *Phys. Rev. E* **109**, 064606 (2024).
- [52] G. Napoli and L. Vergori, *Phys Rev Lett* **108**, 207803 (2012).

Supplemental Material: Integer defects, flow localization, and bistability on curved active surfaces

Rushikesh Shinde¹, Raphaël Voituriez^{2,3}, Andrew Callan-Jones^{1,*}

1 Some basic differential geometry

We briefly define the geometrical quantities that are used in the main text. First, we consider a surface endowed with metric g_{ij} and curvature C_{ij} defined as

$$g_{ij} = \mathbf{e}_i \cdot \mathbf{e}_j \tag{S1}$$

$$C_{ij} = \mathbf{e}_i \cdot \partial_j \mathbf{n}. \tag{S2}$$

In these expressions, the tangent basis is

$$\mathbf{e}_i = \partial_i \mathbf{X}; \tag{S3}$$

partial derivatives are with respect to one of the two coordinates s^i , $i = 1, 2$ parametrizing the surface; and \mathbf{X} is the position vector of a point on the surface in the embedding space. Furthermore, \mathbf{n} is the unit normal vector to the surface, given by

$$\mathbf{n} = \frac{1}{2} \epsilon^{ij} \mathbf{e}_i \times \mathbf{e}_j, \tag{S4}$$

which defines the Levi-Civita tensor ϵ^{ij} . Unit tangent vectors are denoted

$$\hat{\mathbf{e}}_i \equiv \mathbf{e}_i / |\mathbf{e}_i|. \tag{S5}$$

Applying Einstein summation convention, the dual tangent vectors are $\mathbf{e}^i \equiv g^{ij} \mathbf{e}_j$, where g^{ij} is the inverse of the metric. Indices of a tangent vector $\mathbf{a} = a^i \mathbf{e}_i$, or second-rank (enough for our purposes) tensor $\mathbf{A} = A^{ij} \mathbf{e}_i \otimes \mathbf{e}_j$, can be raised or lowered by contraction with g^{ij} or g_{ij} .

Finally, the covariant derivative of a vector \mathbf{a} is defined as $\nabla_i a^j = \mathbf{e}^j \cdot \partial_i \mathbf{a}$, and can be expressed in terms of the Christoffel symbols, $\Gamma_{ij}^k = \mathbf{e}^k \cdot \partial_i \mathbf{e}_j$, as

$$\nabla_i a^j = \partial_i a^j + \Gamma_{ik}^j a^k. \tag{S6}$$

Note that the above definition assumes that \mathbf{a} is a vector that is tangent to the surface.

2 Derivation of ψ dynamics : Equation 7 in the main text

We next provide details on the derivation of Equation 7 in the main text, which describes the dynamics of the orientation angle ψ on an axi-symmetric surface.

Parameterization of a surface using in-plane co-ordinates : An axi-symmetric surface can be parameterized by using in-plane polar co-ordinates: arc length s and azimuthal angle θ ; see Fig. 1 of the main text. Using these parameters, the position vector of a point on this surface in the standard Cartesian basis can be defined as $\mathbf{X} = [r(s)\cos(\theta), r(s)\sin(\theta), z(s)]^T$. From the definition of arc length s , it follows that $z'(s)^2 + r'(s)^2 = 1$, where primes denote differentiation with respect to s . Using the definitions given in Sec. 1 the tangent vectors are

$$\mathbf{e}_\theta = [r'(s)\cos(\theta), r'(s)\sin(\theta), z'(s)]^T, \tag{S7}$$

$$\mathbf{e}_s = [-r(s)\sin(\theta), r(s)\cos(\theta), 0]^T. \tag{S8}$$

28 The metric tensor $g_{ij} = \mathbf{e}_i \cdot \mathbf{e}_j$ and the Levi-Civita tensor $\epsilon_{ij} = \mathbf{n} \cdot (\mathbf{e}_i \times \mathbf{e}_j)$ are given by

$$g_{ij} = \begin{bmatrix} 1 & 0 \\ 0 & r(s)^2 \end{bmatrix} \quad \text{and} \quad \epsilon_{ij} = \sqrt{g} \begin{bmatrix} 0 & 1 \\ -1 & 0 \end{bmatrix}. \quad (\text{S9})$$

29 Here, we have used g as shorthand notation for the determinant of the g_{ij} matrix. In a contravariant basis,
30 the above tensors are written as

$$g^{ij} = \begin{bmatrix} 1 & 0 \\ 0 & 1/r(s)^2 \end{bmatrix}, \quad \epsilon^{ij} = \frac{1}{\sqrt{g}} \begin{bmatrix} 0 & 1 \\ -1 & 0 \end{bmatrix}. \quad (\text{S10})$$

31 Next, the normal vector \mathbf{n} is given by

$$\mathbf{n} = [-z'(s)\cos(\theta), -z'(s)\sin(\theta), r'(s)]^T \quad (\text{S11})$$

32 and the curvature is given by

$$C_{ij} = \begin{bmatrix} r'(s)z''(s) - z'(s)r''(s) & 0 \\ 0 & r(s)z'(s) \end{bmatrix}. \quad (\text{S12})$$

33

34 Finally, in computing the covariant derivative of a tangent vector \mathbf{a} the only non-zero Christoffel symbols
35 are

$$\Gamma_{\theta s}^{\theta} = \frac{r'(s)}{r(s)}, \quad \Gamma_{\theta\theta}^s = -r'(s)r(s). \quad (\text{S13})$$

36 **Dynamics of a +1 active defect :** We next consider the polarity dynamics associated with a +1 defect
37 in an active polar fluid surface. The defect center is found along the axis of symmetry of the surface, i.e., at
38 $s = 0$. Assuming rotational symmetry, the polarity field can be written as

$$\mathbf{p} = \sin(\psi(s, t)) \hat{\mathbf{e}}_s + \cos(\psi(s, t)) \hat{\mathbf{e}}_{\theta} \quad (\text{S14})$$

39 and the flow field, which is orthoradial and axi-symmetric, is

$$\mathbf{v} = v^{\theta}(s, t) \mathbf{e}_{\theta}. \quad (\text{S15})$$

40 The dynamics of the polarity vector is described by the following equation (Eq. 5 in the main text) :

$$\frac{D\mathbf{p}}{Dt} = \frac{\mathbf{h}}{\gamma} - \nu(\mathbf{u} \cdot \mathbf{p}). \quad (\text{S16})$$

41 Here, the co-rotational Lagrangian derivative is $D\mathbf{p}/Dt = \partial\mathbf{p}/\partial t + \mathbf{v} \cdot \nabla\mathbf{p} - \boldsymbol{\omega} \times \mathbf{p}$. On the right hand side
42 of the above equation, the first term includes the molecular field $\mathbf{h} = -\delta F/\delta\mathbf{p}$ and the rotational viscosity
43 γ . The second term represents the coupling between the polarity dynamics and the velocity field, where ν
44 is known as the flow-alignment parameter—which is dimensionless—, and $\mathbf{u} = (\nabla\mathbf{v} + \nabla\mathbf{v}^T)/2$ is the strain
45 rate tensor. Due to the assumed symmetry of the flow profile, Eq. S15, the only non-zero component of \mathbf{u} is
46 the shear component, $u^{\theta s}$. With the aid of Eq. S6, this component can be simplified as follows:

$$\begin{aligned} u^{\theta s} &= \frac{1}{2} (\nabla^s v^{\theta} + \nabla^{\theta} v^s), \\ &= \frac{1}{2} \left(\partial_s v^{\theta} + \frac{r'}{r} v^{\theta} - \frac{r'r}{r^2} v^{\theta} \right), \\ &= \frac{1}{2} \partial_s v^{\theta}. \end{aligned} \quad (\text{S17})$$

47 Next, we project Eq. S16 along \mathbf{p} and the perpendicular tangent direction $\mathbf{p} \times \mathbf{n}$. This gives

$$\mathbf{p} \cdot \frac{D\mathbf{p}}{Dt} = \frac{h_{\parallel}}{\gamma} - \nu\mathbf{p} \cdot (\mathbf{u} \cdot \mathbf{p}), \quad (\text{S18})$$

$$(\mathbf{p} \times \mathbf{n}) \cdot \frac{D\mathbf{p}}{Dt} = \frac{h_{\perp}}{\gamma} - \nu(\mathbf{p} \times \mathbf{n}) \cdot (\mathbf{u} \cdot \mathbf{p}). \quad (\text{S19})$$

48 Here, we have defined h_{\parallel} and h_{\perp} via $\mathbf{h} = h_{\perp}(\mathbf{p} \times \mathbf{n}) + h_{\parallel}\mathbf{p}$. Since the fluid is assumed to be deep in the
 49 ordered state, we have $|\mathbf{p}| = 1$. This implies $\mathbf{p} \cdot D\mathbf{p}/Dt = 0$. This identity can be used to simplify the
 50 equation (S18), which gives

$$h_{\parallel} = \nu\gamma\sqrt{g}u^{\theta s}\sin(2\psi). \quad (\text{S20})$$

51 Equation (S19) can then be simplified as follows. The left-hand side is explicitly given by

$$(\mathbf{p} \times \mathbf{n}) \cdot \frac{D\mathbf{p}}{Dt} = \frac{\partial\psi}{\partial t} + (\mathbf{p} \times \mathbf{n}) \cdot (\mathbf{v} \cdot \nabla\mathbf{p}) - (\mathbf{p} \times \mathbf{n}) \cdot (\boldsymbol{\omega} \times \mathbf{p}) \quad (\text{S21})$$

$$= \frac{\partial\psi}{\partial t} + (\mathbf{p} \times \mathbf{n}) \cdot (v^{\theta}\nabla_{\theta}p^j\mathbf{e}_j) + \boldsymbol{\omega} \cdot \mathbf{n}, \quad (\text{S22})$$

52 In order to simplify the second term on the right hand side above, we first write $\mathbf{p} \times \mathbf{n}$ as $= -\sin(\psi)\hat{\mathbf{e}}_{\theta} +$
 53 $\cos(\psi)\hat{\mathbf{e}}_s$. Then, with the expression for \mathbf{p} , Eq. S14, and some algebra, this term is shown to be equal to
 54 $-v^{\theta}r'$. The third term on the right hand side of the above equation, with the definition of the vorticity
 55 $\omega_n = \boldsymbol{\omega} \cdot \mathbf{n} = \epsilon_{ij}\nabla^i v^j/2$ yields $\omega_n = v^{\theta}r' + \sqrt{g}u^{s\theta} = (r^2v^{\theta})'/2r$. These considerations lead to

$$(\mathbf{p} \times \mathbf{n}) \cdot \frac{D\mathbf{p}}{Dt} = \frac{\partial\psi}{\partial t} + \frac{\sqrt{g}}{2}\partial_s v^{\theta} \quad (\text{S23})$$

56 Having thus addressed the left hand side of Eq. S19, we next tackle the right hand side. A straightforward
 57 calculation gives $(\mathbf{u} \cdot \mathbf{p}) \cdot (\mathbf{n} \times \mathbf{p}) = \cos(2\psi)u^{\theta s}\sqrt{g}/2$. Substituting this expression into Eq. S19 and using
 58 Eq. S23, we obtain

$$\frac{\partial\psi}{\partial t} = \frac{h_{\perp}}{\gamma} - \sqrt{g}\left(1 + \nu\cos(2\psi)\right)u^{s\theta}. \quad (\text{S24})$$

59 From this equation, we can obtain an autonomous dynamical equation for the angle ψ , provided we can
 60 express the shear rate $u^{s\theta}$ as a function of ψ . To do so, we neglect the friction between the liquid film and
 61 the substrate, which, given the axi-symmetry of the problem, implies that the shear deviatoric tension $t^{s\theta}$
 62 vanishes (see main text). By noting that this quantity is given by

$$t^{s\theta} = 2\eta u^{s\theta} + \zeta\Delta\mu p^{\theta}p^s + \frac{\nu}{2}\left(p^{\theta}h^s + p^s h^{\theta}\right) + \frac{1}{2}\left(h^s p^{\theta} - h^{\theta} p^s\right), \quad (\text{S25})$$

63 (see main text, Eq. 4), and writing the molecular field as

$$\mathbf{h} = (h_{\parallel}\cos(\psi) - h_{\perp}\sin(\psi))\hat{\mathbf{e}}_{\theta} + (h_{\parallel}\sin(\psi) + h_{\perp}\cos(\psi))\hat{\mathbf{e}}_s, \quad (\text{S26})$$

64 we obtain

$$2\eta u^{s\theta} = -\frac{\zeta\Delta\mu}{2\sqrt{g}}\sin(2\psi) - \frac{\nu}{2\sqrt{g}}h_{\parallel}\sin(2\psi) - \frac{1}{2\sqrt{g}}\left(1 + \nu\cos(2\psi)\right)h_{\perp} \quad (\text{S27})$$

65 By plugging in the value for h_{\parallel} from (S20), we now obtain the expression for the strain rate in the form of
 66 ψ .

$$u^{s\theta} = \frac{-1}{4\eta\sqrt{g}\left(1 + \frac{\nu^2\gamma}{4\eta}\sin^2(2\psi)\right)}\left[\left(1 + \nu\cos(2\psi)\right)h_{\perp} + \zeta\Delta\mu\sin(2\psi)\right]. \quad (\text{S28})$$

67 This allows us to eliminate $u^{s\theta}$ from (S24), and we thereby obtain following differential equation describing
 68 the dynamics of a +1 defect :

$$\frac{\partial\psi}{\partial t} = \left[\frac{1}{\gamma} + \frac{(1 + \nu\cos(2\psi))^2}{4\eta\left(1 + \frac{\nu^2\gamma}{4\eta}\sin^2(2\psi)\right)}\right]h_{\perp} + \frac{1 + \nu\cos(2\psi)}{4\eta\left(1 + \frac{\nu^2\gamma}{4\eta}\sin^2(2\psi)\right)}\sin(2\psi)\zeta\Delta\mu. \quad (\text{S29})$$

69 This equation can be written more compactly as

$$\frac{\partial\psi}{\partial t} = \frac{1}{\tilde{\gamma}(\psi)}h_{\perp} + \frac{\zeta\Delta\mu}{4\tilde{\eta}(\psi)}(1 + \nu\cos(2\psi))\sin(2\psi), \quad (\text{S30})$$

70 where

$$\tilde{\gamma}(\psi)^{-1} = \frac{1}{\gamma} + \frac{(1 + \nu \cos(2\psi))^2}{4\eta \left(1 + \frac{\nu^2 \gamma}{4\eta} \sin^2(2\psi)\right)} \quad \text{and} \quad \tilde{\eta}(\psi) = \eta \left(1 + \frac{\nu^2 \gamma}{4\eta} \sin^2(2\psi)\right). \quad (\text{S31})$$

71 Note that both $\tilde{\gamma}$ and $\tilde{\eta}$ are positive. If we use the chosen form for the free energy F , which is defined in the
72 main text as Eq. 2, the perpendicular field entering Eq. S30 is given by

$$h_{\perp} = -\frac{\delta F}{\delta \psi} = K \nabla^2 \psi + K_{\text{ex}} \left((C_{\theta}^{\theta})^2 - (C_s^s)^2 \right) \frac{\sin(2\psi)}{2}. \quad (\text{S32})$$

73 In Eq (S32), $\nabla^2 \psi$ is a Laplace-Beltrami operator, given by

$$\nabla^2 \psi = \frac{1}{r} \partial_s \left(r \partial_s \psi \right), \quad (\text{S33})$$

74 which holds because of the assumed rotational symmetry of the problem.

75 3 Determination of a velocity from ψ field

76 We next show how the velocity field $\mathbf{v} = v^{\theta} \mathbf{e}_{\theta}$ can be obtained from knowledge of the ψ . First, assuming
77 no-slip boundary condition at the surface edge, i.e., $v^{\theta}(s = s_{\text{max}}) = 0$, integration of Eq. S17 gives

$$v^{\theta} = \int_{s_{\text{max}}}^s 2u^{s\theta} ds'. \quad (\text{S34})$$

78 Writing the flow field in terms of the physical velocity, that is, $\mathbf{v} = v(s, t) \hat{\mathbf{e}}_{\theta}$, we have

$$v(s, t) = r(s) \int_{s_{\text{max}}}^s ds' 2u^{s\theta}. \quad (\text{S35})$$

79 Next, to obtain the steady-state flow $v(s)$, we use Eqs. S28 and S30 to express the flow in terms of ψ :

$$\begin{aligned} v(s) &= -\zeta \Delta \mu r \int_{s_{\text{max}}}^s \frac{\tilde{\gamma}}{2\gamma\tilde{\eta}} \frac{\sin(2\psi)}{r^2} \sqrt{g} ds', \\ &= -2\zeta \Delta \mu r \int_{s_{\text{max}}}^s \frac{\sin(2\psi)}{r^2 [\gamma\nu(\nu + 2\cos(2\psi)) + 4\eta]} \sqrt{g} ds'. \end{aligned} \quad (\text{S36})$$

80 This integral is evaluated numerically to determine the flow profiles; see Figs. 2, 3, 4 and S1, S3, S4, S5.

81 4 Localized flows on a sphero-cylindrical surface

82 Here we present numerical findings showing that the flows observed on a sphero-cylindrical surface decay
 83 exponentially. Moreover, if the length-scale of this decay (denoted as l) is small enough compared to the
 84 length of the cylinder (denoted as L), we find that the flow profile is independent of L . In other words, the
 flow profile is insensitive to how far is the boundary ; see Fig. S1.

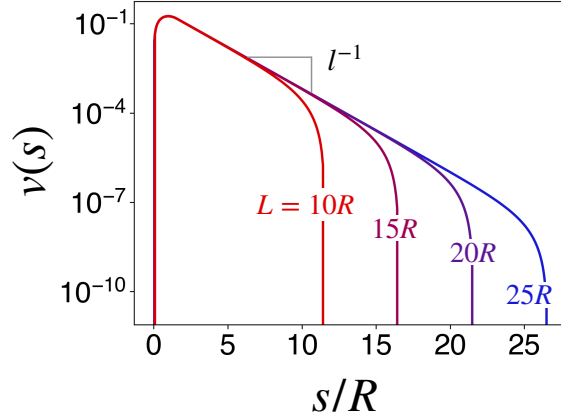


Figure S1: **Localized flow on a sphero-cylindrical surface** : Flow profile, for extensile activity, for different cylinder lengths L , in units of the cylinder radius R . The velocity decays exponentially on the cylindrical surface. Parameters: $\mathcal{Z} = 1.1\mathcal{Z}_c$, $R = 1$, $K_{\text{ex}}/K = 1$, $\nu = -2$, $\eta = \gamma = 1$. Note: \mathcal{Z}_c is defined in the main text.

85

86 5 Passive aster-spiral instability on a hemispherical bump surface

87 We next present numerical results demonstrating that an aster can become passively unstable due to the
 88 influence of deviatoric curvature, \mathcal{D} , leading to a non-trivial spiral solution at equilibrium. In the absence
 89 of extrinsic coupling *i.e.*, $K_{\text{ex}} = 0$, the steady-state passive ψ dynamics equation $h_{\perp} = 0$ simplifies to a
 90 diffusion problem. This admits a constant solution. The value of this solution is dictated by the boundary
 91 conditions. However, the situation is strongly modified for $K_{\text{ex}} \neq 0$.

92 On the skirt region of the bump surface, \mathcal{D} is negative. As discussed in the main text, for $K_{\text{ex}} > 0$, which
 93 is the case we consider throughout, the polarity \mathbf{p} tends to align with \mathbf{e}_{θ} . Therefore, assuming a boundary
 94 condition $\psi(s = s_{\text{max}}) = \pi/2$, the aster is stable. However, this constant solution can become unstable with
 95 sufficiently large extrinsic coupling. In our numerics (solving Eq. 7 of the main text, with $\zeta\Delta\mu = 0$), we
 96 observe a supercritical bifurcation from the aster to a spiral state (see Figs. S2a and S2b). As the value
 97 of K_{ex} increases, the director field aligns more orthoradially. Consequently, for very high values of K_{ex} (or
 98 small ϵ), the orientational order resembles a vortex on the spherical dome.

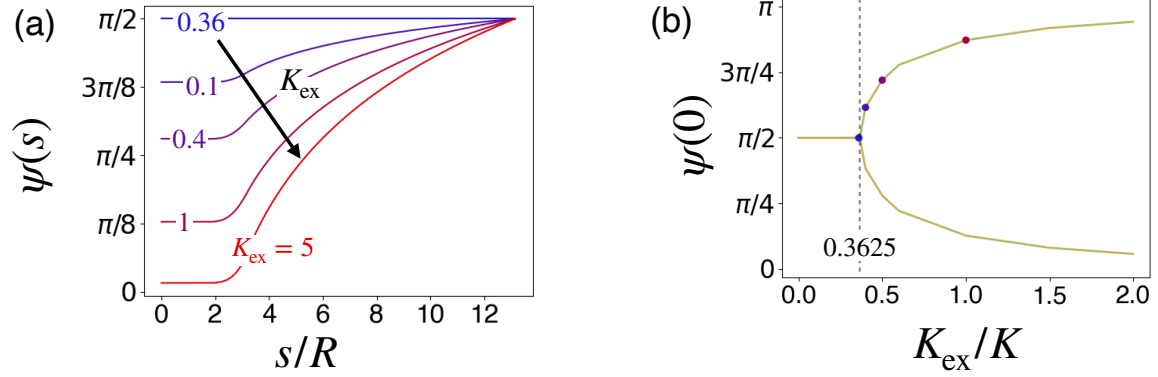


Figure S2: **Supercritical aster-spiral transition at equilibrium.** (a) ψ profile for various values of K_{ex} on the hemispherical bump surface. Note: the threshold value of extrinsic coupling is $K_{\text{ex}} = 0.36$. (b) Pitchfork bifurcation from aster to spiral for increasing K_{ex} . Parameters : $\nu = -2$, $R = \epsilon = 1$, $L = 10R$, $K = 1$.

99 6 Localized flows on the hemispherical bump surface

100 In this section we show that, in contrast to the case of a sphero-cylinder, active flows driven by contractility
 101 can also be localized : the velocity profile is insensitive to how far away the boundary is with respect to the
 102 bump skirt, and it exhibits an exponential decay. While bump surfaces with different values of L (distance
 103 from outer skirt edge to outer boundary of flat surrounding region) will exhibit different passive spiral
 104 solutions, for high enough activity such that the length scale of velocity decay (denoted as l) is smaller than
 105 L , the localized flow profiles that are generated are insensitive to the value of L ; see Fig. S3a. These flows
 106 become more pronounced and localized for increasing contractility, as exhibited by the scaling $l \propto 1/\sqrt{\zeta\Delta\mu}$;
 see Fig. S3b.

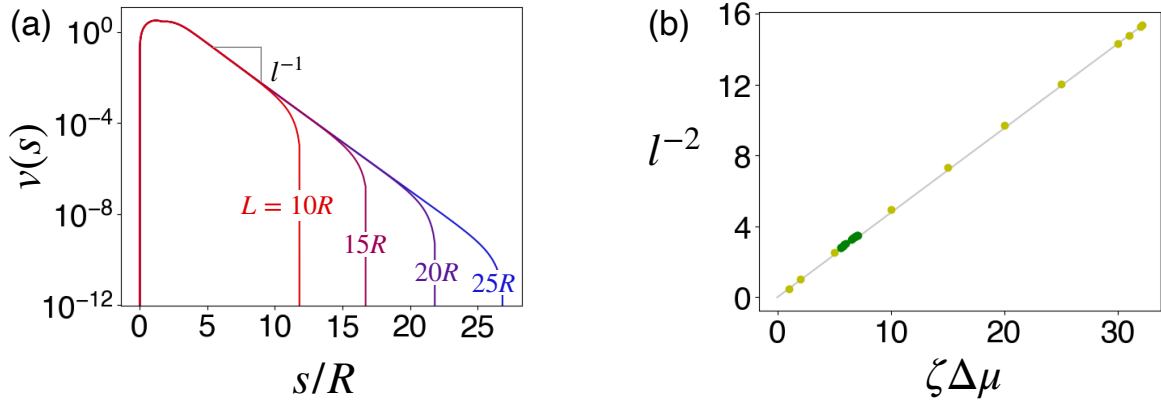


Figure S3: **Contractility-driven localized flow on a hemispherical bump surface :** (a) Flow profiles for different values of L . The velocity profiles decay exponentially on the flat surface. For $l \sim \sqrt{K/\zeta\Delta\mu} \ll L$, $v(s)$ does not depend on L . (b) The rate of the velocity decay is proportional to $\sqrt{\zeta\Delta\mu}$. The yellow points correspond to the yellow line (S1 solutions) and green points correspond to the green line (S2 solutions) in the hysteresis loop shown in Fig. 4a of the main text.

107

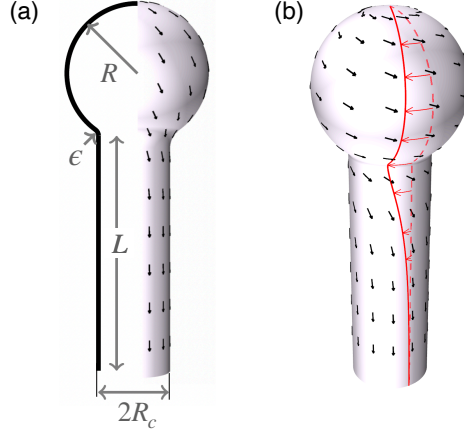


Figure S4: **Localized flows for extensile activity on a bulb-tipped surface.** (a) Schematic representation of a bulb-tipped cylinder. This shows the non-uniform polarity profile (black arrows) at equilibrium. (b) Localized flow for extensile activity, $\zeta\Delta\mu < 0$. The velocity decays exponentially on the cylindrical surface. Parameters : $\zeta\Delta\mu = -2$, $R = 1$, $\epsilon = 0.1$, $R_c = 0.546$, $L = 7$.

7 Results for other surfaces

In this section, we present numerical results for surfaces other than those mentioned in the main text, and which illustrate that the findings obtained there are generic.

7.1 Bulb-tipped cylinder

We consider a bulbed-shaped surface, shown in Fig. S4a, which is combination of types (1) and (2) surfaces. It features a cylindrical base connected to a spherical top via a skirt. Since $\mathcal{D} < 0$ on the skirt, there is an energetic tendency for orthoradial alignment there. Indeed, we observe a passive aster-to-spiral instability for a sufficiently small ϵ , like we did for the hemispherical surface. The non-uniform polarity in the passive state gives rise to threshold-less flows when activity is turned on. These are features we observed for the hemispherical bump (type 2 surface).

Considering the case of $\zeta\Delta\mu < 0$, we find that flows driven by extensile activity on this surface are localized, in line with our findings on the sphero-cylindrical surface, that we identified as a type 1 surface; see Fig. S4b. This confirms that a cylinder-like surface, due to its positive deviatoric curvature, can screen active flows by forcing the orientation field to align along the cylinder's axis (for $K_{\text{ex}} > 0$).

Next, considering the case $\zeta\Delta\mu > 0$, we find that contractility also generates threshold-less, localized flows. High contractility extinguishes these flows and restores the aster, as we observed for the hemispherical bump; see Figs. 3, 4 of the main text and S5. For small ϵ , the spiral-to-aster transition is discontinuous and we observed hysteresis in the v_{max} vs. $\zeta\Delta\mu$ plane, as we saw for the hemispherical bump; see Figs. 4 and S5.

7.2 Bump-function

Finally, to illustrate the generality of the results we obtained in the main text for the fluid on a hemispherical bump, we consider a fluid on a surface of revolution described the so-called *bump function*, which is joined at its edge to a flat surface. The particular bump function we chose is defined by the equation for the height at radial position r :

$$z(r) = H \exp\left(-\frac{1}{1-r^2}\right) \quad 0 \leq r < 1 \quad (\text{S37})$$

$$z(r) = 0 \quad 1 \leq r \leq 1 + L, \quad (\text{S38})$$

131 where the height of the top of the bump is $z(0) = H/e$. We choose $H = e, L = 3, K_{\text{ex}}/K = 1, K =$
 132 1. For this set of parameters, we readily observe passive aster-spiral instability. Similar to case of the
 133 hemispherical surface (main text), we observe localized flows for contractile activity, a discontinuous spiral-
 134 to-aster transition as well as bistability between two different flowing spiral solutions (S1 and S2) and a
 135 discontinuous transition from S2 to S1 (data not shown here).

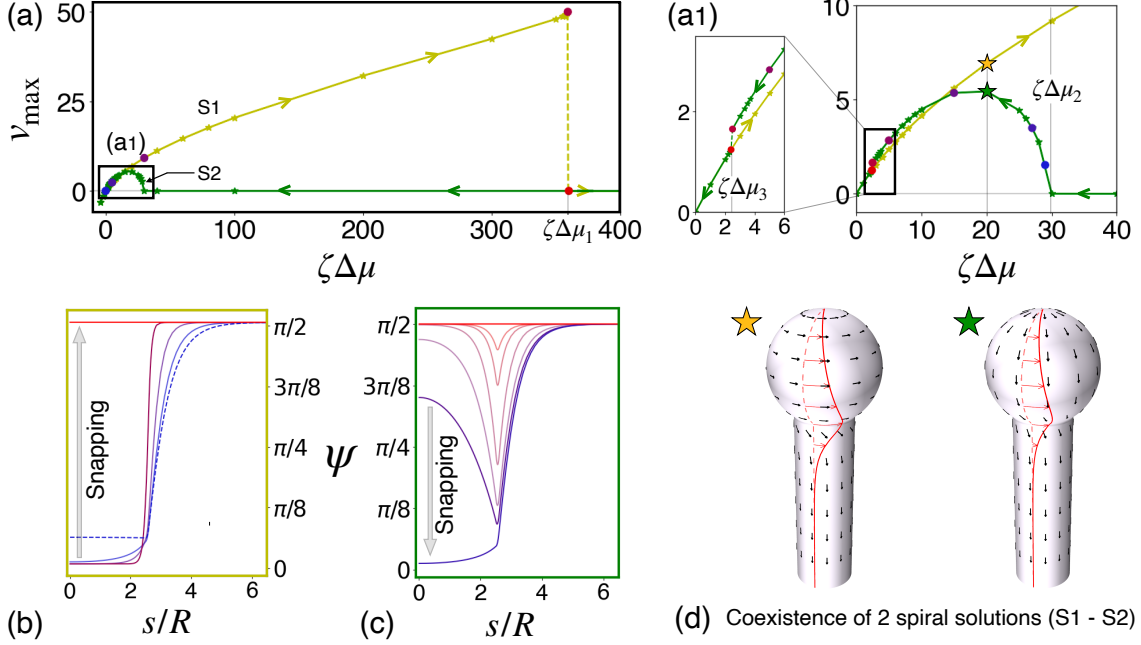


Figure S5: **Bistability of spiral and aster states on a bulb-tipped cylinder** (a) Hysteresis loop for v_{max} versus contractility. (b) The $\psi(s)$ profiles for increasing contractility, color-coded according to the points on the yellow curve in (a), show a discontinuous spiral-to-aster transition. (c) The $\psi(s)$ profiles, color-coded according to the points on green curve (a1), show a continuous aster-to-spiral (S2) transition with decreasing $\zeta\Delta\mu$. Reducing the activity further causes a discontinuous spiral-to-spiral (S2 to S1) transition. (e) Close-up of polarity and flow profiles for S1 and S2 spiral states. Parameter values : $R = 1, \epsilon = 0.1, R_c = 0.546, \nu = -2, K_{\text{ex}} = K = 1$.